

# Lawrence Berkeley National Laboratory

LBL Publications

## Title

Substantial optical dielectric enhancement by volume compression in LiAsSe<sub>2</sub>

## Permalink

<https://escholarship.org/uc/item/6q22060g>

## Journal

Physical Review B, 93(19)

## ISSN

2469-9950

## Authors

Zheng, Fan

Brehm, John A

Young, Steve M

et al.

## Publication Date

2016-05-01

## DOI

10.1103/physrevb.93.195210

Peer reviewed

1 **Substantial optical dielectric enhancement by volume compression in LiAsSe<sub>2</sub>**

2 Fan Zheng,<sup>1</sup> John A. Brehm,<sup>1</sup> Steve M. Young,<sup>2</sup> Youngkuk Kim,<sup>1</sup> and Andrew M. Rappe<sup>1</sup>

3 <sup>1</sup>*The Makineni Theoretical Laboratories, Department of Chemistry,*  
4 *University of Pennsylvania, Philadelphia, Pennsylvania 19104-6323, USA*

5 <sup>2</sup>*Center for Computational Materials Science,*  
6 *Naval Research Laboratory, Washington, D.C. 20375, USA*

7 Based on first-principles calculations, we predict a substantial increase in the optical di-  
8 electric function of LiAsSe<sub>2</sub> under pressure. We find that the optical dielectric constant  
9 is enhanced threefold under compression along all three axes by 3%. This enhancement is  
10 mainly due to the dimerization strength reduction of the one-dimensional (1D) As-Se chains  
11 in LiAsSe<sub>2</sub>, which significantly alters the wavefunction phase mismatch between two neigh-  
12 boring chains and changes the transition intensity. By developing a tight-binding model  
13 of the interacting 1D chains, the essential features of the low-energy electronic structure  
14 of LiAsSe<sub>2</sub> are captured. Our findings are important for understanding the fundamental  
15 physics of LiAsSe<sub>2</sub> and provide a feasible way to enhance the material optical response that  
16 can be applied to light harvesting for energy applications.

17

## I. INTRODUCTION

18 The dielectric response, as a fundamental physical property of materials, describes how ma-  
 19 terials respond to an external electric field. In semiconductors, when the applied electric field  
 20 frequency is in the range of visible light, the photon excitation of electronic inter-band transitions  
 21 dominates the total dielectric response, which is described by the optical dielectric function. The  
 22 optical dielectric function is strongly related to other optical properties of the material, including  
 23 light absorption, refraction and non-linear optical responses. Therefore, the enhancement and tun-  
 24 ability of the optical dielectric function of a material are significantly important in various areas,  
 25 such as solar cell, optical devices and sensors. A great deal of research has been done to increase  
 26 the material optical dielectric response. In particular, defects, material doping and surface plas-  
 27 mon induced by metallic nanoparticles have been widely used to increase the optical absorption  
 28 in semiconductors<sup>1-5</sup>. Whereas most of the previous methods rely on the assistance of another  
 29 material, the intrinsic bulk dielectric response enhancement of the light absorber is less studied.

30 Alkali-metal chalcogenides such as KPSe<sub>6</sub>, K<sub>2</sub>P<sub>2</sub>Se<sub>6</sub>, LiAsSe<sub>2</sub>, LiAsS<sub>2</sub> and NaAsSe<sub>2</sub> have been  
 31 synthesized, and their band gaps lie in the visible light region<sup>6</sup>. Since they have spontaneous polar-  
 32 ization, these materials are potential candidates to show the bulk photovoltaic effect<sup>7</sup>. Moreover,  
 33 strong optical second-harmonic generation susceptibility has been observed experimentally and the-  
 34 oretically<sup>6,8,9</sup>. However, the effect of structural distortion on their linear optical responses has not  
 35 been studied<sup>10</sup>, and the structure-property-optical performance relationship is still unclear. In this  
 36 paper, by using a first-principles method, we show that the optical dielectric constant of LiAsSe<sub>2</sub>  
 37 increases threefold by volume compression. More interestingly, As and Se atoms in LiAsSe<sub>2</sub> form  
 38 weakly interacting quasi-one-dimensional atomic chains, of which the dimerization strength can be  
 39 tuned by volume compression. Atomic chains have attracted a great deal of interest, due to their  
 40 one-dimensional nature giving rise to exotic phenomena such as conductivity<sup>11,12</sup>, metal-insulator  
 41 transition<sup>13</sup>, and topological phases<sup>14,15</sup>. Herein, their important roles in light absorption are em-  
 42 phasized. As illustrated by a tight-binding model, the dimerization strength is strongly coupled to  
 43 the relative phases of the gap state wavefunctions between the two neighboring chains. By reducing  
 44 the wavefunction phase mismatch between the chains, the magnitude of transition intensity for the  
 45 transitions near the band edges increase significantly, giving rise to substantial optical dielectric  
 46 function enhancement.

47

## II. COMPUTATIONAL DETAILS

48 Figures 1a and b show the experimental structure (ES) of  $\text{LiAsSe}_2$ <sup>6</sup>. The polar phase of  $\text{LiAsSe}_2$   
 49 has the  $Cc$  space group with the glide plane perpendicular to the lattice vector  $\vec{b}$ . The polarization  
 50 induced by ionic displacement lies in the  $\vec{a}\text{-}\vec{c}$  plane<sup>7</sup>. As shown, the As and Se atoms form distorted  
 51 quasi-one-dimensional atomic chains along the  $\vec{b}$  direction<sup>16</sup>. This chain and its neighboring chains  
 52 form a two-dimensional chain plane (illustrated as the grey plane), and these chain planes are  
 53 separated by Li-Se planes (light purple plane). In the ES, this As–Se chain dimerizes, creating  
 54 alternating As–Se bonds with two different bond lengths.

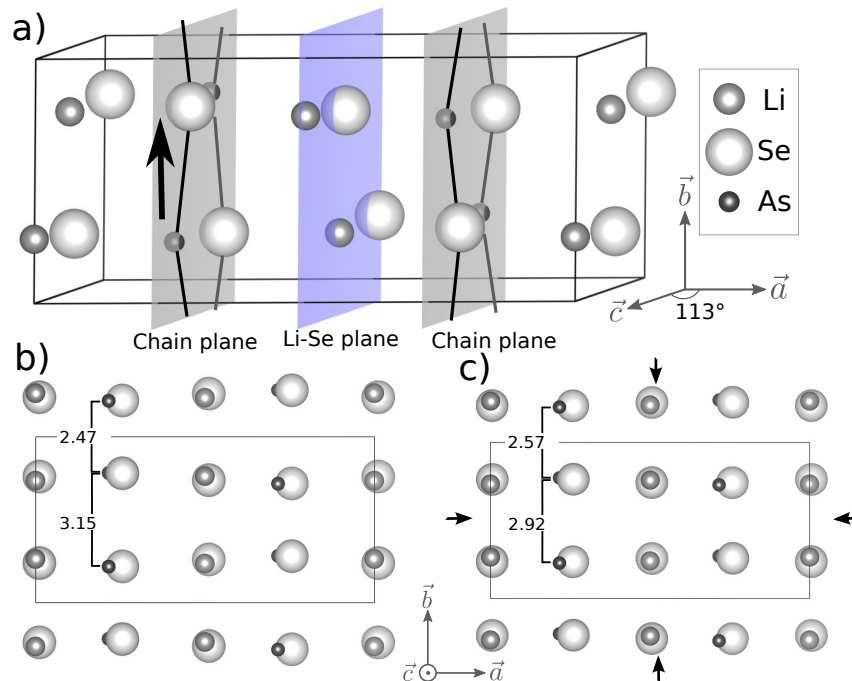


FIG. 1. a) The unit cell of  $\text{LiAsSe}_2$ . The lines between As and Se atoms indicate the quasi-one-dimensional chains. The chain with its neighbor chains form a chain plane (grey color plane). These parallel chain planes are separated by the Li-Se plane (light purple plane) in the middle. b) Side view of the experimental structure (ES). c) Side view of the compressed structure (CS). The differences between the ES and the CS are mainly ion motions in the  $\vec{b}$  direction. As illustrated by the bond lengths between two neighboring As–Se bonds, ES shows stronger dimerization strength along the chain than CS.

55 The plane-wave density functional theory (DFT) package QUANTUM-ESPRESSO was used  
 56 to perform structural relaxations and electronic structure calculations, with the Perdew-Burke-  
 57 Ernzerhof (PBE) generalized gradient approximation exchange-correlation functional<sup>17</sup>. Norm-  
 58 conserving, designed non-local pseudopotentials were generated with the OPIUM package<sup>18,19</sup>. A

59 plane-wave cutoff energy of 50 Ry was sufficient to converge the total energy with the  $k$ -point  
 60 sampling on a  $4 \times 8 \times 8$  grid. The structure relaxed with the PBE functional underestimates the  
 61 dimerization along the chain, and it does not match with the ES. By using the GGA +  $U$  method  
 62 with effective Hubbard  $U_{\text{eff}} = 7.5$  eV on the As 4  $p$  orbitals, the relaxed structure matches the ES  
 63 very well. Adding  $U$  on  $p$  orbitals to get the correct structure is not rare, as the large self-interaction  
 64 error originating from  $s$  or  $p$  orbitals may partially be corrected by the DFT+ $U$  method<sup>20,21</sup>. The  
 65 DFT calculated band gap is 0.8 eV, which underestimates the experimentally measured 1.1 eV<sup>6</sup>.  
 66 With the converged charge density, the wavefunctions used for the dielectric function calculations  
 67 are obtained from non-self-consistent calculations performed on a denser  $k$ -point grid of  $20 \times 36 \times 36$   
 68 and a sufficient number of empty bands (76 empty bands). By using the long wavelength approxi-  
 69 mation and the single particle approximation, the imaginary part of the optical dielectric function  
 70 is calculated as Eq.(1),

$$\epsilon_{2,ii}(\omega) = \frac{\pi}{2\epsilon_0} \frac{e^2}{m^2 (2\pi)^4 \hbar\omega^2} \sum_{c,v} \int_{BZ} d\mathbf{k} |\langle c, \mathbf{k} | p_i | v, \mathbf{k} \rangle|^2 \delta(\omega_{c,\mathbf{k}} - \omega_{v,\mathbf{k}} - \omega) \quad (1)$$

71 where  $\omega$  is the light frequency;  $i$  is the Cartesian coordinate;  $\mathbf{k}$  is the Bloch wave vector;  $c, v$  denote  
 72 the conduction and valence band with energy  $\hbar\omega_{c/v}$ . The real part of the dielectric function,  $\epsilon_1$ ,  
 73 can be calculated from the Kramers-Kronig relation.

### 74 III. RESULTS AND DISCUSSION

75 The compressed structure (CS), with much weaker dimerization strength of the atomic chains  
 76 (Fig. 1c), is obtained by compressing all the lattice vectors by 3%, followed by the relaxation of  
 77 the internal atomic positions<sup>16</sup>. This compression corresponds to approximately 27 kbar stress  
 78 applied almost hydrostatically. The volume compression of LiAsSe<sub>2</sub> strongly enhances its optical  
 79 dielectric response as shown in the calculated optical dielectric functions of the ES and CS (Fig. 2a).  
 80 Furthermore, we find that the dielectric function changes continuously *vs.* applied compression.  
 81 Other compression strengths are also tested as shown in the Appendix Figure.9. Figures 2b, c and  
 82 d illustrate the calculated joint density of states (JDOS), refractive index and absorption spectrum  
 83 along the  $\vec{b}$  direction as a function of the photon energy for the ES and CS, respectively. Two  
 84 other components of the optical dielectric function are also shown in the Appendix Fig.10, showing  
 85 much less enhancement under compression. As shown from the spectrum, the CS shows much  
 86 higher linear optical responses near the band gap than the ES. In particular, the optical dielectric

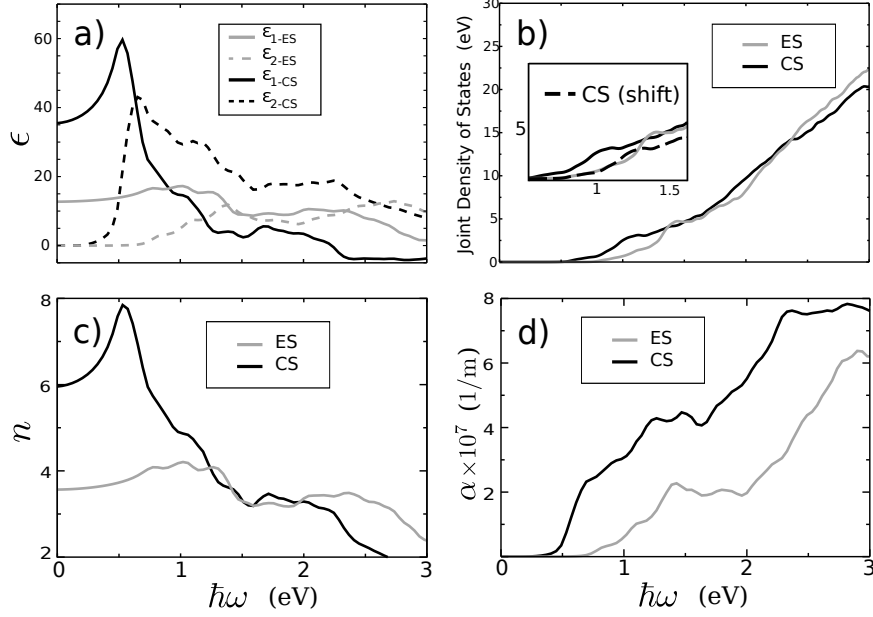


FIG. 2. a) LiAsSe<sub>2</sub> optical dielectric ( $\epsilon$ ) function spectrum of the ES and CS as a function of photon energy along  $\vec{b}$ .  $\epsilon_1$  is the real part of the dielectric response spectrum, and  $\epsilon_2$  is the imaginary part. b) Joint density of states for the two structures. Owing to the different band gaps of the ES and CS (0.2 eV difference), the inset graph shows the shifted-CS (shifting the spectrum by 0.2 eV) and ES JDOS spectra in order to compare with the same band gaps. c) Refractive index ( $n$ ) spectrum along  $\vec{b}$ . d) Absorption coefficient ( $\alpha$ ) spectrum  $\vec{b}$ .

87 constant of the CS increases to more than three times its original value (Fig. 2a). The imaginary  
 88 part of the optical dielectric function, describing the real electronic inter-band transitions, also  
 89 shows great enhancement under compression. As expressed in Equation (1), the imaginary part of  
 90 the dielectric function is the product of JDOS  $\sum_{c,v,\mathbf{k}} \delta(\omega_{c,\mathbf{k}} - \omega_{v,\mathbf{k}} - \omega)$  and the transition intensity  
 91  $|\langle c, \mathbf{k} | p_i | v, \mathbf{k} \rangle|^2$ . However, we find that the JDOS contribution to the enhancement is negligible. As  
 92 shown in Fig. 2b, in the energy range  $0 < \hbar\omega < 2$  eV where the imaginary part  $\epsilon_2$  shows substantial  
 93 enhancement, the calculated JDOS for the ES and CS (shifted) have very similar magnitude. Here,  
 94 we want to emphasize that owing to the different band gaps (0.2 eV) of the ES and CS, the JDOS  
 95 of the CS is shifted by 0.2 eV in order to compare. Therefore, this dielectric function enhancement  
 96 mainly comes from the increase of transition intensity by compression.

97 To further resolve the origin of the dielectric enhancement by pressure, we present the distribu-  
 98 tion of the transition intensity as a function of  $\mathbf{k}$  in momentum space. Figure 3 shows the transition  
 99 intensity distributions in the Brillouin zone (BZ), with the transitions between the valence band  
 100 maximum (VBM) to the conduction band minimum (CBM) within the the energy range of 0–2

101 eV, since these transitions are dominant in the dielectric function enhancement. As displayed in  
 102 Figure 3, the  $k$ -resolved distributions show distinct patterns in addition to their overall differ-  
 103 ences in the corresponding dielectric constants. For the ES, most of the  $\mathbf{k}$  points have similar yet  
 104 low magnitude of transition intensities. However, for the CS, the  $k$ -resolved transition intensity  
 105 shows significant changes, with the high magnitude  $\mathbf{k}$  points mostly distributed on a thin plane  
 106 perpendicular to the reciprocal lattice vector  $\vec{k}_b$ . The  $\mathbf{k}$  points contributing the highest transition  
 107 intensities are broadly located in the middle region in this plane. Along the  $\vec{k}_a$  and  $\vec{k}_c$  directions  
 108 of this plane, the transition intensity changes slowly with respect to wavevectors, indicating the  
 109 weak bonding character. This can be attributed to the weak As/Se–Se/Li inter-planar and As–Se  
 110 inter-chain interactions. However, the magnitude of transition intensity shows rapid change along  
 111 the  $\vec{k}_b$  direction, as illustrated by the transition intensity profile along this direction (Fig. 7b).  
 112 This strong  $k$ -dependent transition intensity distribution reveals the strong covalent bonds char-  
 113 acter along the chain direction. The highly inhomogeneous distribution of the transition intensity  
 114 can be considered as an indication of the quasi one-dimensional nature of the system near the  
 115 low-energy spectrum, stemming from the dimerization changes of the As and Se atoms. Further-  
 116 more, the structural inhomogeneity leads to anisotropic optical responses as shown by the other  
 117 two components of the dielectric functions (Appendix Fig.10), where only the dielectric response  
 118 along chain direction is enhanced significantly when applying compression. Therefore, investigating  
 119 the electronic structure of the chains is essential to further understand the origin of the dielectric  
 120 response enhancement.

121 Figure 4 shows the DFT band structures plotted along  $\Gamma$ –Y. Under compression, most bands  
 122 along the  $\vec{k}_b$  direction show relatively small changes, except the bands near the band edges. The  
 123 CS shows strong dispersion near its optical gap at (0.0, 0.42, 0.0) (fractional coordinate), as its  
 124 CBM shows a “dip” while the VBM shows a “bump”. The ES has its band gap shifted towards  
 125 the BZ boundary at (0.0, 0.46, 0.0). Comparing to those of the CS, the bands of the ES near  
 126 the band gap shows much less dispersion, and the dip and bump features become less obvious.  
 127 Besides the band dispersion change, the band gap shows noticeable change from 0.80 eV (ES) to  
 128 0.62 eV (CS). More importantly, we find that the inter-band transition between the band edges  
 129 in the CS provides the highest transition intensity magnitude, but this corresponding value in  
 130 the ES is very low. In order to understand the bonding characters of these states which give  
 131 the highest transition intensity, the charge density iso-surfaces of the VBM and CBM are plotted  
 132 in Figure 4. Unexpectedly, both the ES and CS show quite similar charge density distributions,  
 133 with non-bonding Se  $p$  orbital character as VBMs and non-bonding As  $p$  as CBMs, suggesting

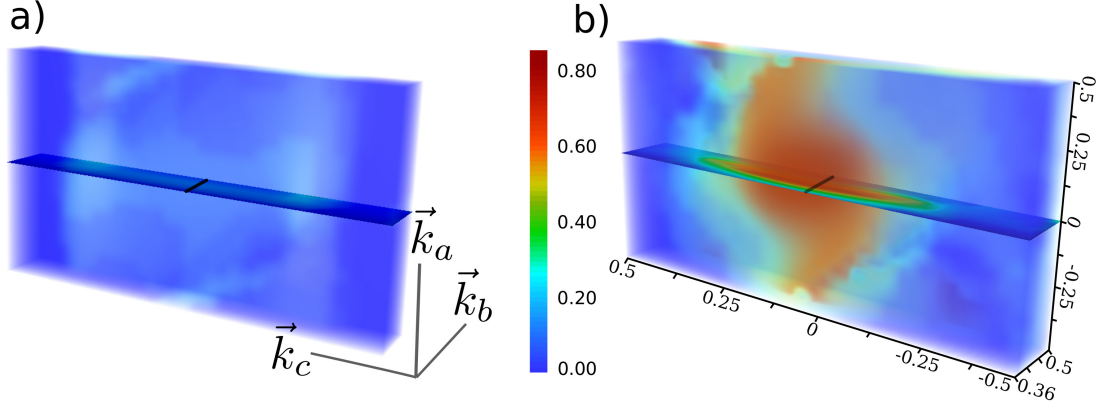


FIG. 3. Distribution of  $|\langle\psi_{v,\mathbf{k}}|\mathbf{p}|\psi_{c,\mathbf{k}}\rangle|^2/V$  ( $\text{eV}/\text{\AA}^3$ ) in the Brillouin zone (BZ) extracted from DFT calculation of  $\text{LiAsSe}_2$  for a) the ES and b) CS.  $V$  is the volume of the unit cell. For simplicity, the primitive BZ is illustrated as an orthogonal box with reciprocal lattice vectors  $\vec{k}_a$ ,  $\vec{k}_b$ , and  $\vec{k}_c$  along the three edges of the box. The transitions with transition energy less than 2 eV are plotted, as this energy region shows the greatest dielectric function enhancement. The detailed transition intensity profiles along the black lines in the figures for the ES and CS are shown in Fig. 7b.

134 that the atomic orbital overlaps cannot explain such large dielectric enhancement by compression  
 135 due to their similar charge densities. Rather, we find that the dimerization change induced by  
 136 the compression can strongly alter the phase of wavefunctions so as to vary transition intensity  
 137 magnitude significantly, as we will discuss below.

138 To demonstrate the significant influence of wavefunction phase change on the optical response  
 139 enhancement, we construct a two-dimensional (2D) tight-binding (TB) model with interacting  
 140 atomic chains illustrated in Figure 5a. The TB model comprises four orbitals ( $i, j = 1, 2, 3, 4$ ) in  
 141 a square lattice with lattice constant  $a$  and periodic boundary conditions along  $\vec{b}$  and  $\vec{c}$  to model  
 142 a chain plane in  $\text{LiAsSe}_2$ . Owing to the weak interaction between the chain plane and the Se–Li  
 143 plane, the inter-planar interaction along the  $\vec{a}$  direction is not considered. As shown in the charge  
 144 density distributions (Fig. 3) and the projected density of states (see Fig. 6 and Appendix Fig.8),  
 145 the  $p$  orbitals from the As and Se atoms are crucial and they form  $\sigma$ -type covalent bonds along the  
 146 chain (along the  $\vec{b}$  direction). Thus, the TB Hamiltonian can be written as:

$$H(\mathbf{k}) = \sum_i \left( \epsilon_i c_{i,\mathbf{k}}^\dagger c_{i,\mathbf{k}} \right) + \sum_{\langle i,j \rangle} \left( t_{ij} c_{i,\mathbf{k}}^\dagger c_{j,\mathbf{k}} + \text{c.c.} \right) \quad (2)$$

147 where  $\epsilon$  is the onsite energy and  $t$  is the hopping strength between nearest orbitals  $i$  and  $j$ . In this



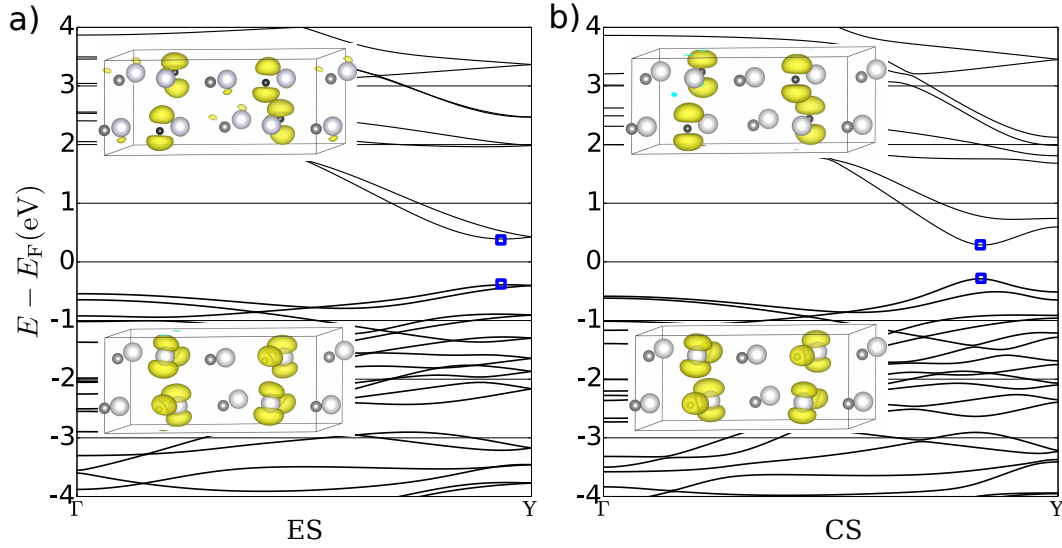


FIG. 4. The band structure of LiAsSe<sub>2</sub> from  $\Gamma$  to Y ( $0, \pi/b, 0$ ) along  $\vec{k}_b$ , and the charge density iso-surfaces of the conduction band minimum (CBM) and valence band maximum (VBM) states indicated by the blue squares in the band structures for a) ES and b) CS.

148 Hamiltonian, the onsite energies of As and Se orbitals are set to  $E_0 + \delta E$  and  $E_0 - \delta E$ , respectively.  
 149 The dimerized hopping strength is denoted as  $t_1 \pm \delta t_1$  to describe the alternating As–Se bond  
 150 lengths. By compression, the dimerization is reduced, leading to more even As–Se neighboring  
 151 bond length along the chain, and the smaller  $\delta t_1$  magnitude. Across the chains ( $\vec{c}$ -direction),  $\pi$ -  
 152 bonding between the  $p$  orbitals forms, where the corresponding hopping interaction is denoted as  
 153  $t_2 \pm \delta t_2$ . We find that this inter-chain interaction is of crucial importance in reproducing the correct  
 154 DFT band structure, although these interactions are weak relative to the intra-chain interaction,  
 155 thus assuming  $|t_2| < |t_1|$ . The onsite energies and hopping strengths of the TB Hamiltonian are  
 156 tuned to reproduce the DFT band structure near the band edges.

157 By solving the TB model numerically, we obtain the band structures in Fig. 5c plotted along  
 158 the chain propagation direction indicated by the blue line in Fig. 5b. We also calculate the band  
 159 structures by gradually reducing the dimerization strength (decreasing  $\delta t_1$ ) with  $t_2$  fixed, and find  
 160 that the band gap position shifts away from the BZ boundary. Furthermore, the As  $p$  and Se  $p$   
 161 atomic orbital projections in DFT and the TB model are compared for the valence and conduction  
 162 band as shown in Fig. 6. The TB model calculation shows the same orbital hybridization and the  
 163 trend of change under compression to DFT, validating the TB model we use. In addition, the  
 164 maximally-localized Wannier functions are computed for the ES and CS structures<sup>22</sup>. Their onsite

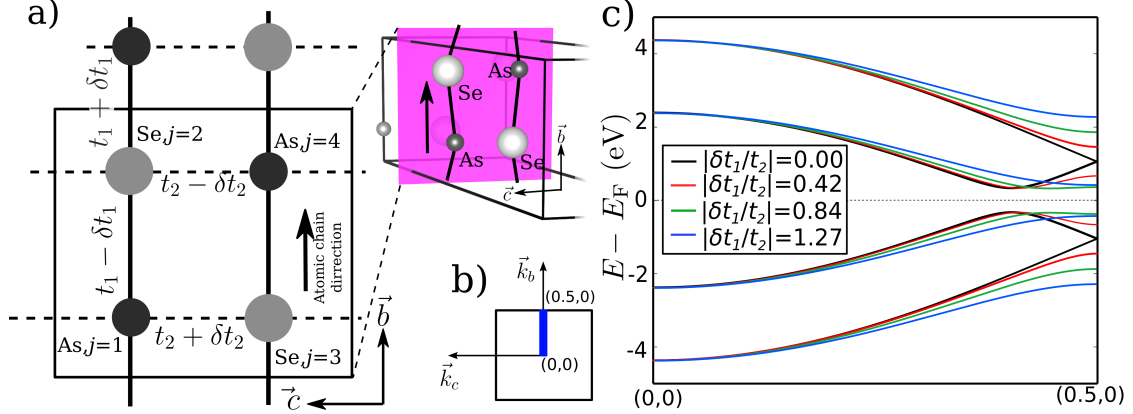


FIG. 5. a) 2D TB model for weakly interacting As–Se chains (the inset graph shows the chains in  $\text{LiAsSe}_2$ ). The dashed lines indicate the chain-chain interaction connecting the As–Se chains (solid lines).  $t \pm \delta t$  denotes the hopping strength. b) The Brillouin zone of the 2D model. The band structure (graph c) is plotted along the thick blue line. c) The band structure calculated from the 2D TB model along the chain propagation direction under different dimerization strengths ( $\delta t_1/t_2$  with  $t_2$  fixed).

165 energies and hopping strengths also fall into the range of the TB model in this work. From the  
 166 TB band structure, the dispersion of the band edges are significantly enhanced when decreasing  
 167  $\delta t_1$ . This feature becomes clearer by calculating the  $k$ -resolved transition intensity using the TB  
 168 wavefunctions.

169 As derived in the Appendix, the transition intensity ( $\mathcal{I}$ ) is expressed as  $\mathcal{I}(\mathbf{k}) = |W^{v,c}(\mathbf{k}) \Pi(\mathbf{k})|^2$ ,  
 170 with  $W^{v,c} = \sum_{j,j'} C_{j',\mathbf{k}}^{v*} C_{j,\mathbf{k}}^c$ , summing over the contributions of the wavefunction coefficients to the  
 171 transition intensity. In this case,  $\Pi$  accounts for the contribution generated when constructing  
 172 the TB basis set from the localized atomic orbitals, with its relative value only determined by  
 173 the wavevector without solving the Hamiltonian. Shown in Fig. 7 is the calculated  $\mathcal{I}$  along the  
 174 same  $k$ -path as used in the TB band structure (Fig. 5b). By reducing the dimerization strength of  
 175 the atomic chains (reducing  $\delta t_1/t_2$ ), the transition intensities for the band edge states and nearby  
 176 increase significantly, which agrees well with the DFT transition intensity trend under compression  
 177 shown in Fig. 7b. Additionally, by plotting  $W$  which is contributed only from the wavefunction as  
 178 we are interested, it is clear that it shows exactly the same trend as  $\mathcal{I}$ , demonstrating the significant  
 179 role of wavefunctions in the enhancement of the transition intensity under pressure.

180 The low-energy  $k \cdot p$  effective theory provides simpler and more explicit band structure and  
 181 wavefunction expression. The Hamiltonian  $H(\mathbf{k})$  is further expanded in the vicinity of the BZ  
 182 boundary as  $H(\mathbf{k}) = H(\mathbf{K}) + (\mathbf{k} - \mathbf{K})H'(\mathbf{K})$  with  $\mathbf{k} = \mathbf{K} + (q, 0)$ ,  $\mathbf{K} = (\pi/b, 0)$ . From the  $k \cdot p$   
 183 Hamiltonian, the energies for the valence band ( $E_-$ ) and the conduction band ( $E_+$ ) near the BZ

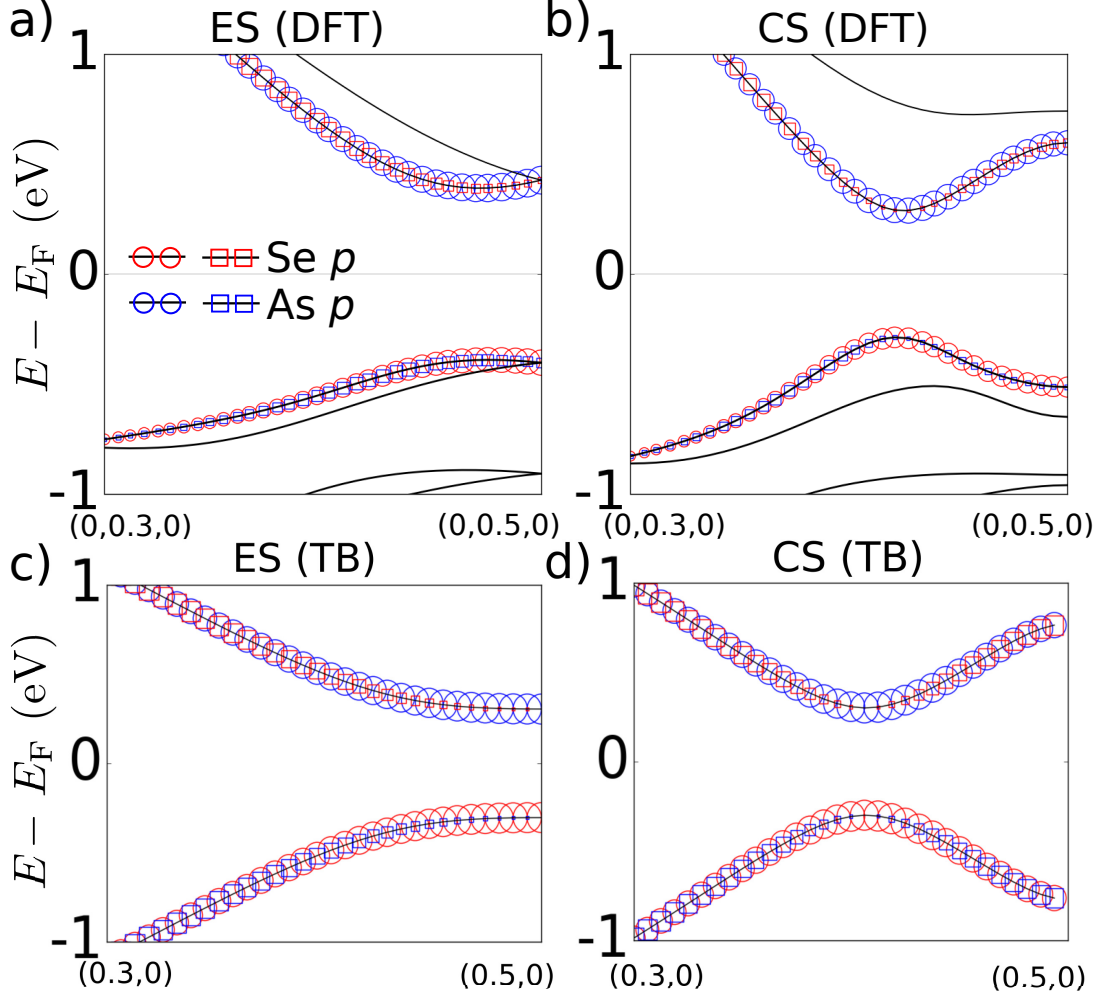


FIG. 6. The Bloch wavefunction projection onto the Se  $p$  and As  $p$  orbitals along the bands for a) ES by DFT, b) CS by DFT, c) ES by TB and d) CS by TB. The size of the circle and square represents the atomic orbital contribution weight.

184 boundary are obtained as:

$$E_{\pm}(q) = \pm \sqrt{\delta E^2 - 2\sqrt{4t_2^2\Omega(q) + 4\delta t_2^2} + \Omega(q)} \quad (3)$$

$$\Omega(q) = 4\delta t_1^2 + (qat_1)^2 \quad (4)$$

185 When  $|\delta t_1| > |t_2|$ , the band gap is at the BZ boundary ( $q = 0$ ). By decreasing the dimerization  
 186 strength such as  $|\delta t_1| < |t_2|$ , the band gap wavevector ( $q(E_g)$ ) is  $2\sqrt{t_2^2 - \delta t_1^2}/(at_1)$ . This change of  
 187 band gap position as a function of the dimerization strength ( $\delta t_1/t_2$ ) agrees with our DFT band  
 188 structures of LiAsSe<sub>2</sub>. In the ES, the strong dimerization between the As and Se atoms moves the  
 189 band gap close to the BZ boundary. In the CS, the reduced dimerization due to the compression

190 shifts the band gap away from the boundary, giving rise to the strong dispersion for the states near  
191 the gap.

192 Within this low energy theory, the phase relationships of the wavefunctions are further explored  
193 by evaluating the analytical expression of wavefunctions for the band edge states. When the band  
194 gap is not at the BZ boundary ( $|\delta t_1| < |t_2|$ ), the wavefunctions of the gap states have simple  
195 forms:

$$\psi_{\text{VBM}} = 1/\sqrt{2} \left( 0, e^{i\theta}, 1, 0 \right), \quad (5)$$

$$\psi_{\text{CBM}} = 1/\sqrt{2} \left( 1, 0, 0, e^{i\theta} \right) \quad (6)$$

196

197 where the wavefunctions are written with the TB basis of the four orbitals:  $\chi_{\text{As},j=1}$ ,  $\chi_{\text{Se},j=2}$ ,  $\chi_{\text{Se},j=3}$ ,  
198 and  $\chi_{\text{As},j=4}$  (Fig. 5a). Due to the simple form of the wavefunctions, we use these two states to show  
199 the effect of phases of the chains. Here,  $\theta = \arcsin(|\delta t_1/t_2|)$  indicates the dimerization strength  
200 of the atomic chains. From the wavefunction expression, it is clear that the VBM and CBM are  
201 always non-bonding states without mixing of the As and Se orbitals, which is also observed in the  
202 DFT calculation. More interestingly,  $\theta$  controls the phase mismatch between the wavefunctions  
203 of the two chains in the chain plane. For example, for the CBM wavefunction, when  $\theta = 0$ ,  
204 the orbitals on  $\chi_{\text{As},j=1}$  and  $\chi_{\text{As},j=4}$  are populated in the same phase, while, with nonzero  $\theta \neq 0$ ,  
205  $\chi_{\text{As},j=1}$  on one chain and  $\chi_{\text{As},j=4}$  on the neighboring chain have the phase difference of  $e^{i\theta}$  between  
206 the corresponding wavefunction coefficients. Hence, the application of the hydrostatic stress to  
207  $\text{LiAsSe}_2$  reduces  $\theta$ , enabling wavefunction phase matching between the two neighboring atomic  
208 chains, which is essential to the enhancement of dielectric responses.

209 Using this simple form of wavefunctions, the band edge transition intensity is evaluated as  
210  $\mathcal{I} \propto |e^{i\theta} + e^{-i\theta}|^2 = \cos^2(\theta) = 1 - (\delta t_1/t_2)^2$ . The first exponential term  $e^{i\theta}$  originates from one  
211 chain and the other term from the neighboring chain. In this material, the finite dimerization  
212 strength of the two neighboring chains have opposite effects to their contributions to the transition  
213 intensity. Therefore, without varying the overlaps between the atomic orbitals, the phase change  
214 of the wavefunction induced by structural change alters the overall dielectric function significantly.

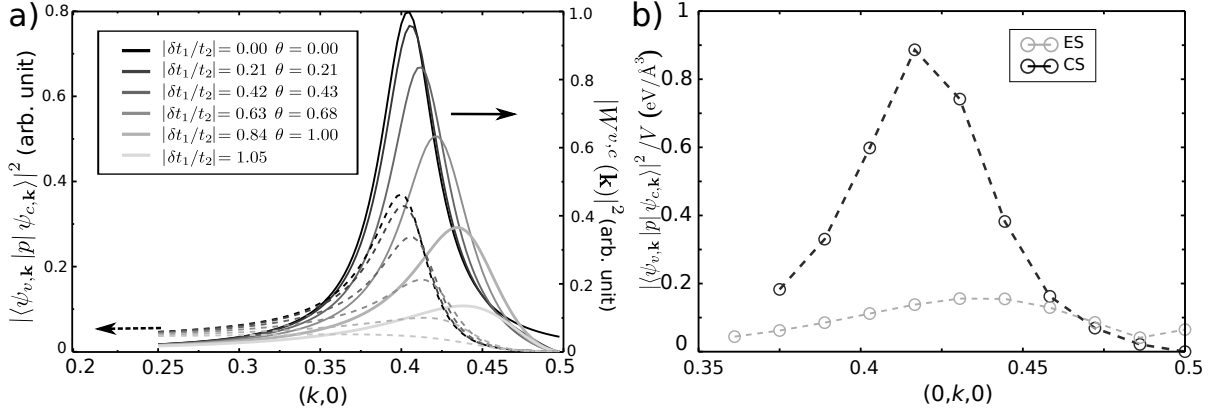


FIG. 7. a) Calculated transition intensities  $\mathcal{I}(\mathbf{k})$  and  $|W^{v,c}(\mathbf{k})|^2$  ( $W^{v,c}(\mathbf{k}) = \sum_{j,j'} C_{j',\mathbf{k}}^{v*} C_{j,\mathbf{k}}^c$ ) from 2D TB model. The  $x$  axis is the wavevector along the chain direction. b) Transition intensities (eV/Å<sup>3</sup>) extracted from DFT calculation of transition intensity for the ES and CS. They are plotted along the chain direction as indicated by the short black lines in Fig. 3.

215

#### IV. CONCLUSION

216 In summary, by using a first-principles method, we have shown that volume compression can  
 217 significantly enhance the optical dielectric function and the dielectric constant by factor of three  
 218 in LiAsSe<sub>2</sub>. This material is essentially a network of As–Se 1D atomic chains with the dimer-  
 219 ization strength tunable by compression. The enhancement of the transition intensity near band  
 220 edges is the main reason of the overall dielectric function improvement. A 2D tight-binding model  
 221 with weakly interacting atomic chains is developed to explore the relation of dimerization strength  
 222 and transition intensity. When the dimerization is strong, the wavefunctions of the two neighbor-  
 223 ing chains have significant phase mismatch, providing destructive interference that reduces to the  
 224 dielectric function. By reducing this wavefunction phase mismatch via compression, the collec-  
 225 tive contributions from the chains dramatically enhance the overall dielectric response and light  
 226 absorption. Our results indicate that this material is suitable as the light absorber in the solar  
 227 cell application. Furthermore, since the transition intensity is related to other optical processes  
 228 such as second-harmonic generation and the non-linear optical effects, we expect that the volume  
 229 compression can enhance their responses.

230

#### V. ACKNOWLEDGMENT

231 F.Z. was supported by the Department of Energy under grant DE-FG02-07ER46431. J.A.B.  
 232 was supported by the National Science Foundation under grant DMR-1124696. S.M.Y. was sup-

ported by the Office of Naval Research under grant N00014-11-1-0664. Y.K. was supported by the National Science Foundation under grant DMR-1120901. A.M.R. was supported by the Office of Naval Research under grant N00014-12-1-1033. The authors acknowledge computational support from the HPCMO of the DOD and the NERSC center of the DOE.

## APPENDIX

### Transition intensity and TB model

The Bloch wavefunction based on the TB orbitals is:

$$\psi_{n,\mathbf{k}} = \sum_j C_j^{n,\mathbf{k}} \chi_j^{\mathbf{k}} \quad (\text{A.7})$$

$\chi_j^{\mathbf{k}}$  ( $j=1, 2, 3,$  and  $4$ ) is expanded as  $\sum_{\mathbf{R}} e^{i\mathbf{k}\cdot(\mathbf{R}+\mathbf{s}_j)} \phi_{\mathbf{R},j}$ , and  $\phi_{\mathbf{R},j}$  is the localized atomic orbital centering at the position of  $\mathbf{R} + \mathbf{s}_j$ .

With the Bloch wavefunctions, the transition intensity is expressed as:

$$\begin{aligned} \mathcal{I}(\mathbf{k}) &= |\langle \psi_{v,\mathbf{k}} | \mathbf{p} | \psi_{c,\mathbf{k}} \rangle|^2 \\ &= \left| \sum_{j,j'} C_{j',\mathbf{k}}^{v*} C_{j,\mathbf{k}}^c \Pi_{jj',x}(\mathbf{k}) \right|^2 \end{aligned} \quad (\text{A.8})$$

where  $\Pi_{j,j'}(\mathbf{k}) = e^{i\mathbf{k}\cdot(\mathbf{s}_j-\mathbf{s}_{j'})} \sum_{\bar{\mathbf{R}}} e^{i\mathbf{k}\bar{\mathbf{R}}} \langle \phi_{-\bar{\mathbf{R}},j'} | \mathbf{p} | \phi_{0,j} \rangle$  with summation over nearest hopping neighbor unit cells denoted by  $\bar{\mathbf{R}}$ , which is only related to the wavevector, orbital position and the momentum matrix element between two localized atomic orbitals.

The low energy Hamiltonian is written as:

$$H(q) = \begin{bmatrix} E & i2\delta t_1 - qat_1 & 2t_2 & 0 \\ -i2\delta t_1 - qat_1 & -E & 0 & 2t_2 \\ 2t_2 & 0 & -E & i2\delta t_1 - qat_1 \\ 0 & 2t_2 & -i2\delta t_1 - qat_1 & E \end{bmatrix}$$

with respect to the four orbitals shown in Figure 5. Based on this Hamiltonian, the band edge states can be solved as Equations 4 and 5.

When calculating the transition intensity for band edge transitions, the transition intensity can be further simplified as:

$$\begin{aligned}
\mathcal{I}(q) &= |C_{j'=1,q}^{v*} C_{j=0,q}^c \Pi_{j=0,j'=1} + C_{j'=2,q}^{v*} C_{j=3,q}^c \Pi_{j=3,j'=2}|^2 \\
&= |e^{i\theta} + e^{-i\theta}|^2 |\Pi(q)|^2 \\
&\equiv |W^{v,c}(q)|^2 |\Pi(q)|^2
\end{aligned} \tag{A.9}$$

252 In this model,  $\Pi_{j=0,j'=1} = \Pi_{j=3,j'=2}$ . The transition intensity is only related to the wavefunction  
253 coefficient  $C$  and the wavefunction phase mismatch between two neighboring chains.

### 254 Projected density of states

255 Fig.8 shows the projected density of states (PDOS) for the ES and CS. For the states near the  
256 band gap,  $p$  orbitals from Se and As are dominant to the valence bands and conduction bands.  
257 Hence, these two types of orbitals are crucial and considered in the tight-binding (TB) model.

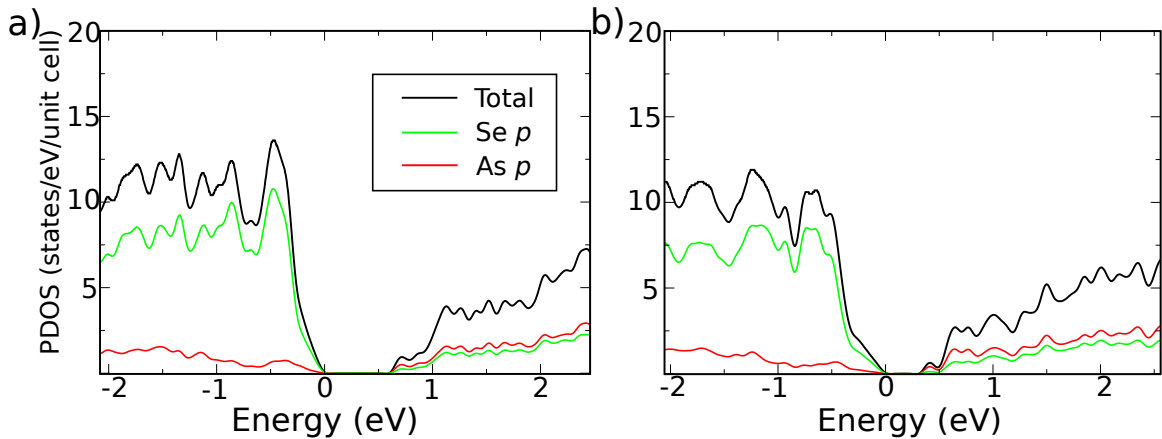


FIG. 8. The projected density of states (PDOS) of the a) ES and b) CS. The band gap states are mainly Se  $p$  and As  $p$  orbital characters.

### 258 Continuous Change of Optical Dielectric under Pressure

259 In the main text, 3% compression is shown illustrating the enhancement of the optical dielectric  
260 function. However, this compression induced enhancement is continuous under the pressure. Shown  
261 in Fig.9 is the optical dielectric functions under the different compression as 1%, 2%, 3% and 4%  
262 (corresponding to the stress 7.1, 14.5, 27.0 and 42.0 kbar, respectively). The dielectric constant  
263 is continuously enhanced under the compression as shown in Fig.9 b). Although the smaller band  
264 gaps due to the stronger compression contribute to the dielectric constants, the imaginary parts of  
265 the optical dielectrics are showing significant increase under the compressions.

### 266 $XX$ and $ZZ$ Components of the Optical Dielectric

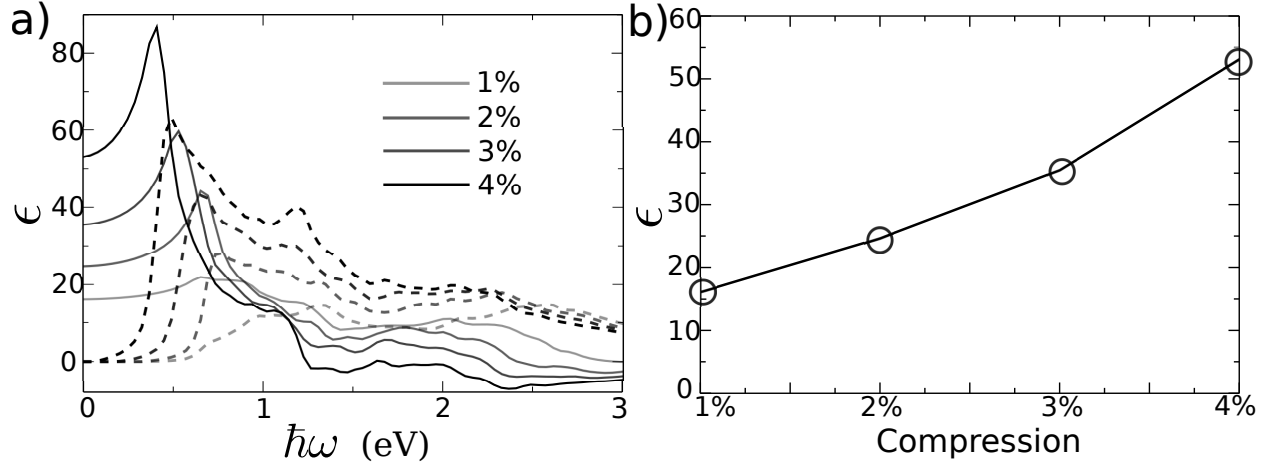


FIG. 9. a) Optical dielectric functions under different compressions. b) The enhancement of the dielectric constants under different compressions.

267 LiAsSe<sub>2</sub> shows strong anisotropy of the optical dielectric function in the three directions owing  
 268 to the different bonding properties along the three axis as shown in Fig.10. This anisotropy is  
 269 significantly enhanced under the compression as  $yy$  (same to  $bb$ , used in the main text) component  
 270 shows great increase. This further originates from the special electronic structure in the  $y$  direction  
 271 (same to  $\vec{b}$  direction). In particular, the polarization on  $a - c$  plane distinguishes the bonding  
 272 properties along  $\vec{a}$  and  $\vec{c}$  for the band edges. However, the enhancement of  $xx$  and  $zz$  are much  
 273 less significant compared to the  $yy$  (same to  $bb$ ) component shown in Fig.10 for the ES and CS.  
 274 Here, we want to clarify that  $x, y$  and  $z$  are along the Cartesian axis. Thus, the  $x$  direction is the  
 275 same to the  $\vec{a}$  direction, however,  $z$  direction is slightly different from the  $\vec{c}$  direction.

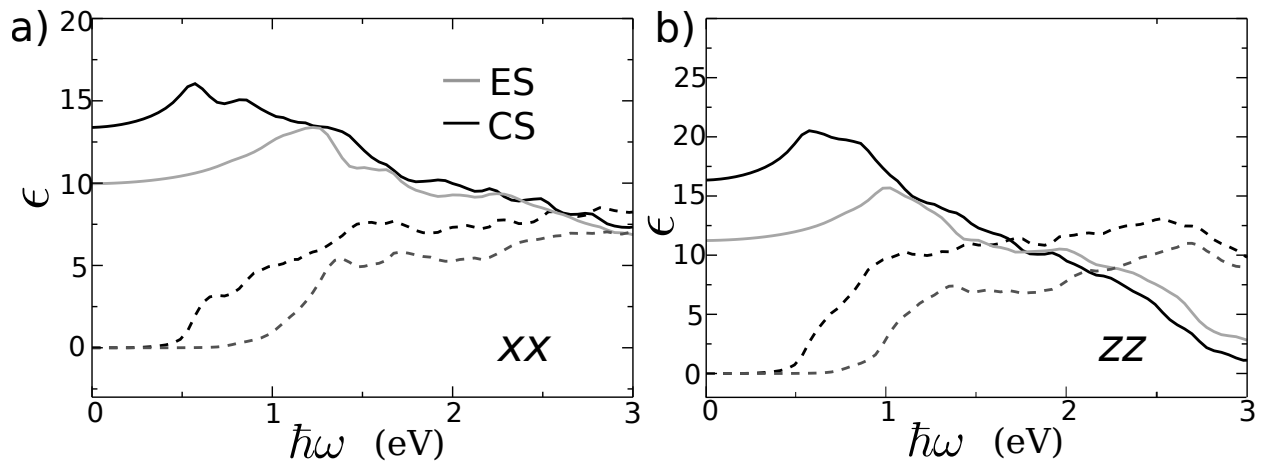


FIG. 10. a) Optical dielectric functions in  $xx$  component of the ES and CS. b) Optical dielectric functions in  $zz$  component of the ES and CS.



- 
- 276 <sup>1</sup> M. Chikamatsu, T. Taima, Y. Yoshida, K. Saito, and K. Yase, *Applied physics letters* **84**, 127 (2004).  
277 <sup>2</sup> D. M. Schaadt, B. Feng, and E. T. Yub, *Appl. Phys. Lett.* **86**, 063106 (2005).  
278 <sup>3</sup> F. Beck, A. Polman, and K. Catchpole, *Journal of Applied Physics* **105**, 114310 (2009).  
279 <sup>4</sup> P. K. Santra and P. V. Kamat, *Journal of the American Chemical Society* **134**, 2508 (2012).  
280 <sup>5</sup> L. Li, W. Wang, H. Liu, X. Liu, Q. Song, and S. Ren, *The Journal of Physical Chemistry C* **113**, 8460  
281 (2009).  
282 <sup>6</sup> T. K. Bera, J. I. Jang, J.-H. Song, C. D. Malliakas, A. J. Freeman, J. B. Ketterson, and M. G. Kanatzidis,  
283 *Journal of the American Chemical Society* **132**, 3484 (2010).  
284 <sup>7</sup> J. A. Brehm, S. M. Young, F. Zheng, and A. M. Rappe, *J. Chem. Phys.* **141**, 204704 (2014).  
285 <sup>8</sup> J.-H. Song, A. J. Freeman, T. K. Bera, I. Chung, and M. G. Kanatzidis, *Physical Review B* **79**, 245203  
286 (2009).  
287 <sup>9</sup> B.-L. Ni, H.-G. Zhou, J.-Q. Jiang, Y. Li, and Y.-F. Zhang, *Acta Physico-Chimica Sinica* **26**, 3052 (2010).  
288 <sup>10</sup> K. Gulyamov, L. VA, T. NA, and V. Fridkin, *Doklady Akademii Nauk SSSR* **161**, 1060 (1965).  
289 <sup>11</sup> O. Cretu, A. R. Botello-Mendez, I. Janowska, C. Pham-Huu, J.-C. Charlier, and F. Banhart, *Nano*  
290 *Letters* **13**, 3487 (2013).  
291 <sup>12</sup> X. F. Wang, C. Roncaioli, C. Eckberg, H. Kim, J. Yong, Y. Nakajima, S. R. Saha, P. Y. Zavalij, and  
292 J. Paglione, *Phys. Rev. B* **92**, 020508 (2015).  
293 <sup>13</sup> A. L. Torre, A. Botello-Mendez, W. Baaziz, J. C. Charlier, and F. Banhart, *Nat Comms* **6**, 6636 (2015).  
294 <sup>14</sup> M. A. Farhan, G. Lee, and J. H. Shim, *Journal of Physics: Condensed Matter* **26**, 042201 (2014).  
295 <sup>15</sup> J. A. Steinberg, S. M. Young, S. Zaheer, C. L. Kane, E. J. Mele, and A. M. Rappe, *Phys. Rev. Lett.*  
296 **112**, 036403 (2014).  
297 <sup>16</sup> “See Supplemental Material at [] for the detailed lattices and the atomic positions of the experimental  
298 and the compressed structures.”.  
299 <sup>17</sup> P. Giannozzi, S. Baroni, N. Bonini, M. Calandra, R. Car, C. Cavazzoni, D. Ceresoli, G. L. Chiarotti,  
300 M. Cococcioni, I. Dabo, A. D. Corso, S. de Gironcoli, S. Fabris, G. Fratesi, R. Gebauer, U. Gerstmann,  
301 C. Gougoussis, A. Kokalj, M. Lazzeri, L. Martin-Samos, N. Marzari, F. Mauri, R. Mazzarello, S. Paolini,  
302 A. Pasquarello, L. Paulatto, C. Sbraccia, S. Scandolo, G. Sclauzero, A. P. Seitsonen, A. Smogunov,  
303 P. Umari, and R. M. Wentzcovitch, *J. Phys.: Condens. Matter* **21**, 395502 (2009).  
304 <sup>18</sup> A. M. Rappe, K. M. Rabe, E. Kaxiras, and J. D. Joannopoulos, *Phys. Rev. B Rapid Comm.* **41**, 1227  
305 (1990).  
306 <sup>19</sup> N. J. Ramer and A. M. Rappe, *Phys. Rev. B* **59**, 12471 (1999).  
307 <sup>20</sup> P. Erhart, A. Klein, D. Åberg, and B. Sadigh, *Phys. Rev. B* **90**, 035204 (2014).  
308 <sup>21</sup> I. Slipukhina, P. Mavropoulos, S. Blügel, and M. Ležaić, *Phys. Rev. Lett.* **107**, 137203 (2011).  
309 <sup>22</sup> A. A. Mostofi, J. R. Yates, Y.-S. Lee, I. Souza, D. Vanderbilt, and N. Marzari, *Comput. Phys. Commun.*  
310 **178**, 685 (2008).